Chin. Sci. Bull. (2014) 59(21):2638–2646
DOI 10.1007/s11434-014-0377-4

Article

Engineering Thermophysics

The bubble leakage mechanism for vertical upflows by the phase separation concept

Qicheng Chen · Jinliang Xu · Dongliang Sun

Received: 6 January 2014 / Accepted: 13 February 2014 / Published online: 8 May 2014

Abstract Recently, our research group proposed the phase separation condenser tube, in which a mesh cylinder was inserted to form the flow structure of "gas near the tube wall and liquid in the tube core", significantly enhance the condensation heat transfer. But the bubble leakage towards the core region may worsen the heat transfer enhancement. In order to prevent the bubble leakage, the critical criterion was proposed based on the Young–Laplace equation, considering the inertia force, viscous force and pulsating flow. It was found that the critical criterion depends on the dimensionless parameter G^*, the We number and a coefficient C. The numerical model was developed in terms of the volume of fluid method to predict the two-phase laminar flow in the phase separation condenser tube. The results show that the bubble leakage takes place at the bubble tip, which is agreed with the experimental observations. The critical curve distinguishing the non-bubble-breaking and bubble-breaking was obtained by comparing the bubble dynamics at different G^* and We. The coefficient C was determined. The critical criterion for the bubble leakage is given as $G^* \times We = \left(0.22We^{0.99349} - \frac{G^*}{4.7\times10^3\times We^{0.00651}} + \frac{196.39}{We^{0.00651}}\right) \times \frac{4\cos\alpha}{\Delta\Theta W}$, providing the design and operation guidance for the phase separation condenser tube.

Q. Chen · J. Xu (✉)
State Key Laboratory of Alternate Electrical Power System with Renewable Energy Sources, North China Electric Power University, Beijing 102206, China
e-mail: xjl@ncepu.edu.cn

J. Xu · D. Sun (✉)
Beijing Key Laboratory of New and Renewable Energy, North China Electric Power University, Beijing 102206, China
e-mail: dlsun@ncepu.edu.cn

Keywords Phase separation concept · Bubble leakage · Critical criterion · Thin liquid film · Condensation heat transfer · Numerical simulation

1 Introduction

Condensers are widely applied in various industry facilities, including the filmwise and dropwise condensation mechanisms. It is noted that the dropwise condensation heat transfer coefficient is larger than the filmwise condensation heat transfer coefficient by more than ten times. However, the filmwise condensation is difficult to be maintained in a practical condenser [1–3]. Thus, a hot research area is to investigate how to enhance the filmwise condensation heat transfer [4].

Nusselt [5] was the first to propose the theoretical model for the film condensation on the vertical plate. He pointed out that the condensation heat transfer coefficient is sharply decreased with increasing in the liquid film thickness. The theory indicates that the thermal conduction resistance is the major resistance of the heat transfer. Because of this, the reduction of the liquid film thickness is the governing principle to enhance the condensation heat transfer. Since 1970s, various condenser tubes have been invented, such as the micro-fin tubes [6–9], the groove tubes [10, 11] and the tubes with insert, [12] etc. Even though these tubes successfully enhance heat transfer, the following issues exist: (a) the tubes have the flow structure of "gas in the tube core and liquid near the tube wall", having thick liquid film on the tube wall; (b) the tubes obviously increase the flow resistance; (c) the fabrication cost is increased. These factors limit the applications of these tubes.

To solve the thick liquid film issue related to the flow structure of "gas in the tube core and liquid near the tube

wall", Chen et al. [13, 14] invented a new type of condenser tube by suspending a mesh cylinder in a tube. The Chen's invention prevents the gas/vapor bubbles from entering the mesh cylinder insider, enforcing the gas phase flowing in the annular region between the tube wall and the micromembrane surface. The thin liquid film can be formed on the tube wall, and the phase distribution is changed to "gas near the tube wall and liquid in the tube core". The experimental measurements showed that the heat transfer coefficients can be more than two times of those in a bare tube [15–17]. The flow visualizations showed that the mechanism of the enhanced heat transfer consists of the thin liquid film on the tube wall and the self-sustained pulsating flow, for the vertical upflows. In addition to this, it is observed that the bubble tip can be closely contacted with the micromembrane surface for a long slug bubble. The gas-liquid interface breaks through the micro pores of the mesh cylinder to emit miniature bubbles from the bubble tip. Such phenomenon is called the "bubble leakage", which decreases the gas content in the annular region to worsen the heat transfer enhancement amplitude. Thus, it is necessary to develop a criterion to predict the bubble leakage appearance.

In this paper, the three-dimensional mesh screen structure was converted to a two-dimensional one. A hybrid grid system was established and a dynamic coordinate attached on the gas bubble was introduced. These efforts significantly reduce the computation time. The critical condition for the bubble leakage was theoretically analyzed for the phase separation condenser tube (vertical upflow), and the major dimensionless parameters were identified. The numerical model was developed in terms of the VOF (volume of fluid) method to explore the bubble leakage mechanism. The relationship among these parameters was quantified to achieve a new bubble leakage criterion, which is helpful for the design and operation of the phase separation condenser tube.

2 The physical problem and statement

2.1 The geometry configuration

We study the bubble leakage from the annular region to the core region in a phase separation condenser tube, with air-water as the working fluid. Figure 1 shows the phase separation condenser tube with a micromembrane cylinder insert, consisting of four regions: (1) bare tube region, (2) annular region, (3) core region, and (4) mesh pore region. The tube and mesh cylinder had diameters of 15.7 and 10.4 mm, respectively. The inlet average velocity, u_{in}, was 0.1033 m/s. The liquid and gas superficial velocities were J_l = 0.0574 m/s and J_g = 0.0459 m/s. The computation domain had a length l of 300.0 mm. The Reynolds numbers for the two-phases are defined as

$$Re_l = \frac{J_l \rho_l d_e}{\mu_l}, Re_g = \frac{J_g \rho_g d_e}{\mu_g}, \tag{1}$$

in which $Re_l \approx 900$, $Re_g \approx 50$, which are lower than 2,000. Thus, the laminar flow was assumed.

Figure 1b–c shows the three-dimensional mesh structure. There are million mesh pores for a one meter long tube with the mesh wire thickness δ of 0.075 mm and the mesh pore width w of 0.15 mm. It is necessary to perform the 3D to 2D conversion of the mesh screen structure. The equivalent diameter of the mesh pore, flow area of the total mesh pores and the capillary force within the mesh pore were assumed to be identical for the two types of mesh screen structures:

$$w = 2w', \tag{2}$$

$$[w/(w+\delta)]^2 = w'/(w'+\delta'), \tag{3}$$

$$4\sigma\cos\theta/w = 2\sigma\cos\theta/w'. \tag{4}$$

Figure 1d shows the two-dimensional structure, with the equivalent mesh wire thickness δ' of 0.086 mm and the mesh pore width w' of 0.075 mm. The two-dimensional axial-symmetric coordinate is employed. The original coordinate O can be set somewhere inside the mesh cylinder (region 4) where is fully developed.

2.2 Governing equations and nondimensionalization

The VOF method simulates the bubble dynamics in the phase separation condenser tube. The PLIC (Piecewise Linear Interface Construction) method reconstructs the gas-liquid interface. The governing equations are

$$\nabla \cdot \left(\vec{v}\right) = 0, \tag{5}$$

$$\frac{\partial \vec{v}}{\partial t} + \vec{v}\cdot\nabla\cdot\vec{v} = -\frac{1}{\rho}\nabla p + \frac{1}{\rho}\nabla\cdot\left[\mu\left(\nabla\cdot\vec{v} + \nabla\cdot\vec{v}^T\right)\right] + \vec{g} + \frac{1}{\rho}\sigma k\nabla\alpha\frac{\rho}{0.5\left(\rho_l+\rho_g\right)}, \tag{6}$$

$$\frac{\partial \alpha}{\partial t} + \nabla\cdot\left(\vec{v}\,\alpha\right) = 0, \tag{7}$$

where $\vec{v}$ is the velocity vector, t is the time, ρ is the density, μ is the viscosity, α is the volume faction, g is the gravity acceleration, σ is the surface tension, k is the interface curvature. The subscripts l and g denote the liquid and gas phase, respectively. The two-phase properties are calculated as

$$\rho = \rho_l\alpha_l + \rho_g\alpha_g, \tag{8}$$

$$\mu = \mu_l\alpha_l + \mu_g\alpha_g, \tag{9}$$

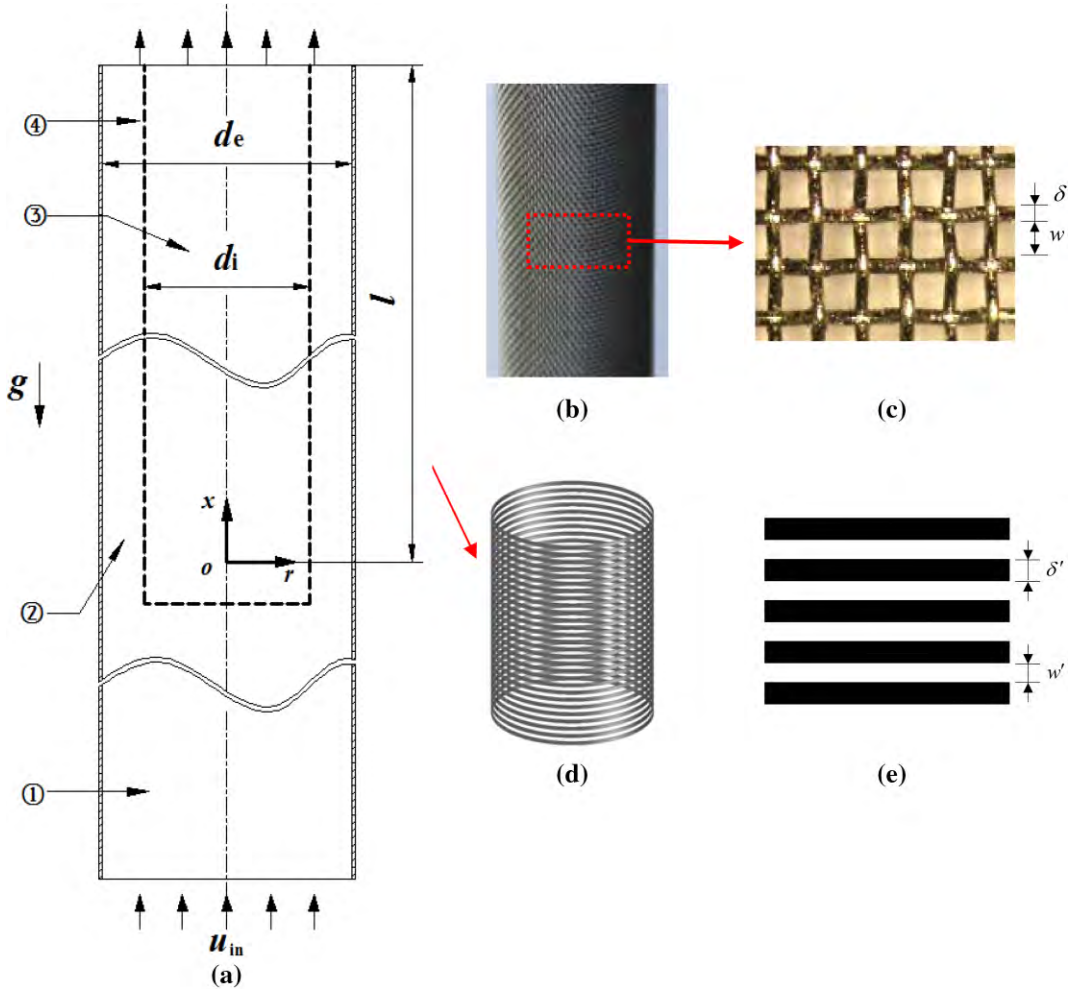

Fig. 1 The phase separation condenser tube

$$\alpha_l + \alpha_g = 1. \tag{10}$$

The non-dimensional parameters are

$$X = \frac{x}{d_e}, R = \frac{r}{d_e}, \tau = \frac{tu_{in}}{d_e}, U = \frac{u}{u_{in}}, V = \frac{v}{u_{in}}, \Theta = \frac{\rho}{\rho_l}, \Psi = \frac{\mu}{\mu_l}. \tag{11}$$

Thus, the governing equations in the dimensionless forms are

$$\nabla \cdot \left(\vec{V}\right) = 0, \tag{12}$$

$$\frac{\partial \vec{V}}{\partial \tau} + \vec{V} \cdot \nabla \vec{V} = -\frac{1}{\Theta}\nabla P + \frac{1}{\Theta}\nabla \cdot \left[\frac{\Psi}{Re}\left(\nabla \cdot \vec{V} + \nabla \cdot \vec{V}^{\mathrm{T}}\right)\right] + \vec{G} + \frac{1}{\Theta We} K \nabla \alpha \frac{\Theta}{0.5\left(\Theta_l + \Theta_g\right)}, \tag{13}$$

$$\frac{\partial \alpha}{\partial \tau} + \nabla \cdot \left(\vec{V}\alpha\right) = 0, \tag{14}$$

where $P = \frac{p}{\rho_l u_{in}^2}, Re = \frac{\rho_l u_{in} d_e}{\mu_l}, We = \frac{\rho_l u_{in}^2 d_e}{\sigma}, G = \frac{g d_e}{u_{in}^2}, K = d_e k$. The symbol ∇ in Eqs. (12)–(14) is calculated in the non-dimensional coordinate.

2.3 Initial and boundary conditions

Figure 2 shows the non-dimensional initial and boundary conditions over the half computation domain.

(1) The initial Taylor bubble size was set. The bubble radius of the bubble front, $R_{TB,}$ is 0.15213. The bubble body length L_{TB} is 2.4458 and the liquid film thickness between the bubble and the wall is 0.0127. The distance from the tube entrance to the bubble tail, L_P, is 1.9108. The whole computation domain had a length L of 19.108, noting that all these parameters are in non-dimensional.

(2) The grid number is decreased from 6.4×10^8 for the 3D mesh structure to 2.79×10^6 for the 2D structure. This grid number still needs much computation cost. Thus, the frame of reference [18, 19] was applied to

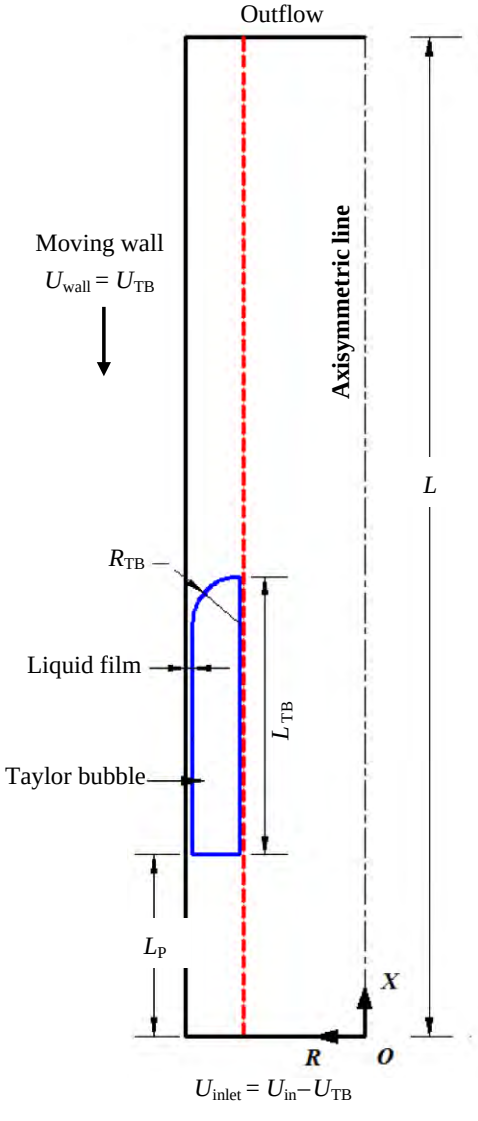

Fig. 2 Initial and boundary conditions

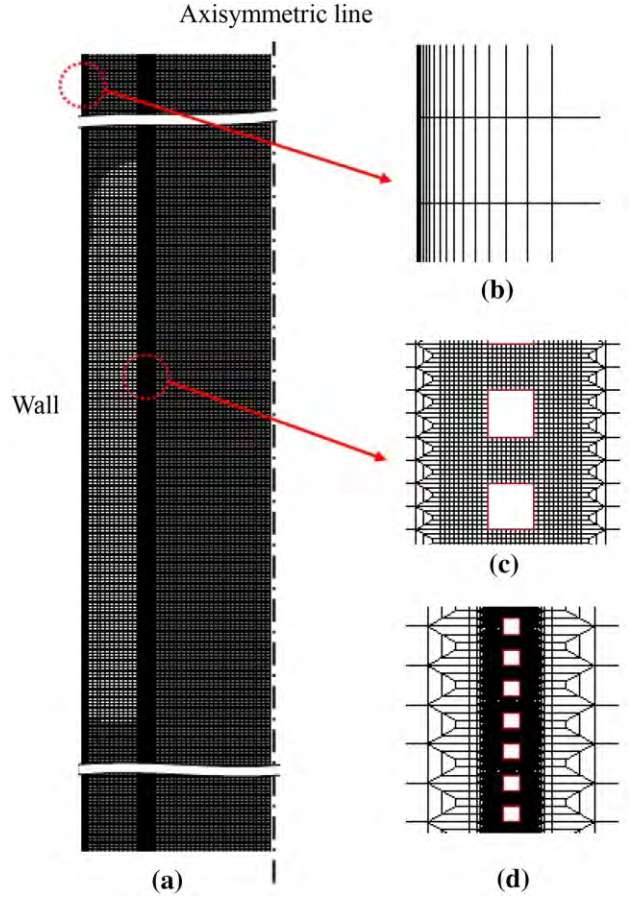

Fig. 3 The multiscale grid system

further reduce the computation cost. The frame of reference was attached on the slug bubble body [18, 19]. Thus, the bubble was stationary relative to the frame of reference. Under such circumstance, the boundary conditions are: the inlet velocity $U_{inlet} = U_{in} - U_{TB}$, the wall moving velocity $U_{wall} = U_{TB}$, where U_{TB} is the bubble rising velocity. At the tube outlet, $\frac{\partial \vec{V}}{\partial X} = 0$. The no-slip boundary condition was applied on the wall.

2.4 The grid generation system

The phase separation condenser tube consisted of three length scales: the bare tube region and core region in macroscale, the annular region in miniature scale and the mesh pores in micron scale (see Fig. 3). The grid number attains tens of millions if the uniform grid system is used. Much computation cost is needed even for the parallel computation of the non-steady bubble dynamics problem with the VOF tracking involved. Thus, different grid scales are applied in terms of different geometry configuration. The near wall region applied the boundary layer type grids with the minimum non-dimensional grid size of 0.0002 (see Fig. 3b). The annular region and core region had the non-dimensional grid size of 0.0113324. The near mesh pore region had the grid size of 4.77×10^{-4} (see Fig. 3c). The different length scales are adapted with each other (see Fig. 3d). The final gird number is reduced from the initial 6.4×10^{8} to 1.06×10^{6} by means of the 3D to 2D conversion criteria, the frame of reference technique and the multiscale grid system.

2.5 Verification of the numerical results

Equations (12)–(13) are solved by the finite volume method and the *SIMPLE* algorithm, in which the momentum terms are with the second order upwind scheme discretization. The simulations are run on a work station having four 8-core CPUs (2.4 GHz each) and 24 GB of RAM. The 8 cases are calculated simultaneously using

Table 1 The verifications

Comparison	Computing time (month)	Length (mm)	Average rising velocity (m/s)	Average liquid film thickness (mm)	Mesh number
Fix frame coordinate	1	52.18485	0.609934	0.078	5.3×10^6
Reference frame coordinate	0.2	51.36031	0.629498	0.081	1.06×10^6
Error		1.58 %	3.21 %	3.84 %	

parallel computing of 32-core. Each case costs about 6 days.

After the verification of the mesh independence, the bubble dynamics in the phase condenser tube were simulated using the fixed frame coordinate and the reference frame coordinate, respectively. Table 1 shows the comparison between them. The average liquid film thickness was 0.078 mm using the fixed frame coordinate and 0.081 mm using the reference frame coordinate, having the relative error of 3.84 %. The average rising velocities of the Taylor bubble were 0.609934 and 0.629498 m/s, having the error of 1.63 %. Besides, the slug bubble lengths were 52.18485 and 51.36031 mm, having the error of 1.53 %. Table 1 proved that the computations using the reference frame coordinate were accurate and reduced the computation time to 20 % of that using the fixed frame coordinate (Table 1).

3 Results and discussion

3.1 Theoretical analysis of the critical criterion of the bubble leakage

The gas-liquid phases are separated by the capillary separation effect on the micromembrane surface in the phase separation condenser tube, forming the phase distribution of "gas near the tube wall and liquid in the tube core". The slug bubble flowing in the annular region should overcome a surface tension force near the mesh pores if the bubble would like to break through the mesh pores. Hung and Lin [20] proposed a surface energy analysis for a bubble breaking through a micro-pore, neglecting the effect of inertia force and viscous force. Here we develop a critical criterion for the bubble leakage in the phase separation condenser tube under various running conditions, considering the effect of the inertia force and viscous force. The flow visualizations indicated the pulsating flow in the phase separation condenser tube [21–23]. The following criterion is developed based on the fact that the gravity force due to the light fluid in the annular region and heavy liquid in the core region should be balanced by the capillary force created by the mesh pores:

$$\Delta\rho g l_{\mathrm{TB}} = C\frac{4\sigma\cos\alpha}{w}, \tag{15}$$

where $\Delta\rho$ is the density difference of liquid and gas, l_{TB} is the bubble length in the annular region, α is connect angle between the bubble and mesh pore surface, w is the mesh pore width and σ is the surface tension. The correction coefficient C considers the effect of the viscosity force, inertia force, etc. The left side of Eq. (15) represents the gravity force sustained on the gas-liquid interface due to the different fluid densities in the core region and annular region. It is observed that the bubble length l_{TB} majorly depends on the mass flow rate of the gas phase and the gravity acceleration. The bubble length will be changed if one changes the gravity acceleration even for the same gas volume to alter the pressure difference across the gas-liquid interface. The right side of Eq. (15) is the capillary force across the gas-liquid interface, in which the term $4\cos\alpha/w$ is determined by the mesh pore size and the contact angle α. Here α is set as 180 [24]. Equation (15) indicates that the bubble leakage takes place when the gravity force due to the density difference in the two regions is larger than the capillary force that can be created within the mesh pores. The nondimensionalization of Eq. (15) yields

$$G^* \times We = C\frac{4\cos\alpha}{\Delta\Theta W}, \tag{16}$$

where $G^* = g l_{\mathrm{TB}}/u_{\mathrm{in}}^2$. Equation (8) indicates that the bubble leakage depends on the non-dimensional parameter G^*, the We number and the coefficient C. A specific criterion is reached once the coefficient C is determined, which will be discussed in the next section.

3.2 Running cases

Totally 77 cases were computed to determine the coefficient C (see Fig. 4). The figure used the axial coordinate of the We number and the vertical coordinate of the dimensionless parameter G^*. The blue and green symbols represent the non-bubble-breaking cases and the bubble-breaking cases, respectively. The non-bubble-breaking and bubble-breaking cases are interfaced obviously on a red curve shown in Fig. 4, indicating that the criterion can be expressed as the function of the parameters of G^* and We. The coefficient C is correlated as

$$C = 0.22We^{0.99349} - \frac{G^*}{4.92 \times 10^3 \times We^{0.00651}} + \frac{187.57}{We^{0.00651}}. \tag{17}$$

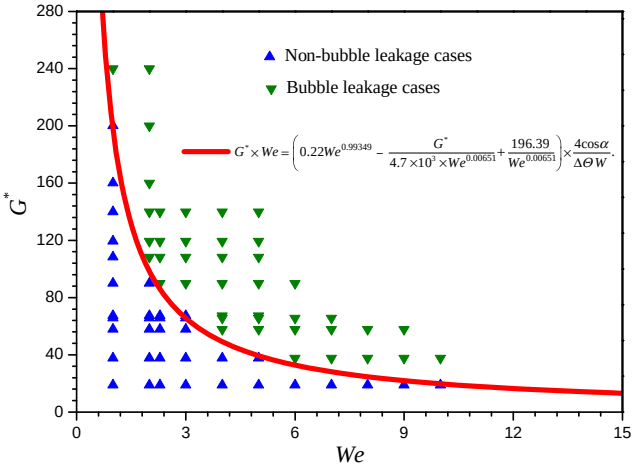

Fig. 4 Running cases and critical curve of the bubble leakage

Substituting Eq. (17) into Eq. (16), the critical criterion for the bubble leakage is expressed as

$$G^* \times We = \left(0.22We^{0.99349} - \frac{G^*}{4.7 \times 10^3 \times We^{0.00651}} + \frac{196.39}{We^{0.00651}}\right) \times \frac{4\cos\alpha}{\Delta\Theta W}. \quad (18)$$

The bubble leakage happens if the left side of Eq. (18) is larger than the right side of Eq. (18). Equation (18) is a general expression for the bubble leakage, which is suitable for the laminar air-water flow system at specific geometry size of the mesh screen. Equation (18) is called the critical criterion for the bubble leakage to predict if the bubble leakage occurs.

3.3 Effect of G^* and We on the bubble dynamics and bubble leakage

Five cases selected from the 77 cases were carefully analyzed (see Table 2). The effect of the parameter G can be explored by comparing cases 1, 2 and 5. Meanwhile, the effect of G^* can be explored by comparing cases 2, 3 and 4. It is noted that the case 2 is for the critical bubble leakage case.

Figure 5 shows the effect of G^* on the bubble shape and flow field at the same We number, in which Fig. 5a–c correspond to the cases 3, 2 and 4. At $G^* = 37.74$, the low

Table 2 The running cases

Case	We	G^*
1	1.00	87.06
2	2.29	87.06
3	2.29	37.74
4	2.29	119.43
5	3.00	87.06

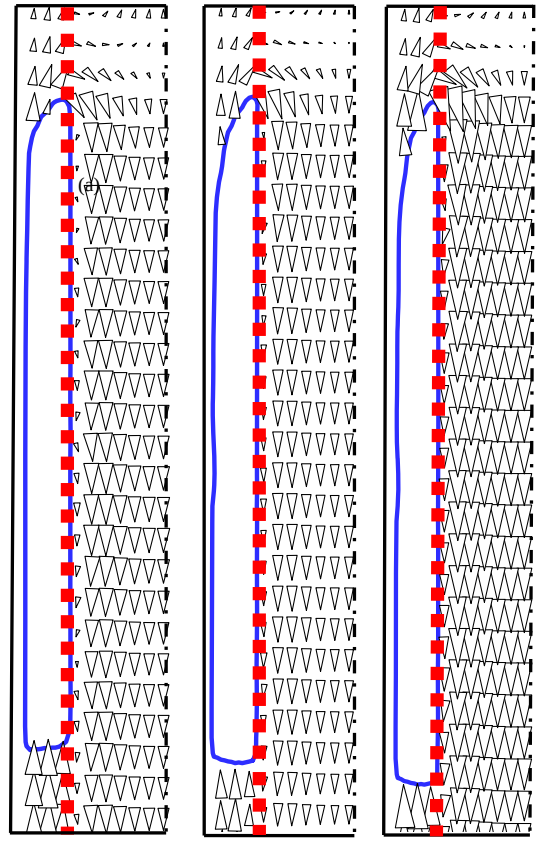

(a) G^*=37.74 **(b)** G^*=87.06 **(c)** G^*=119.43

Fig. 5 The bubble shape and flow field at different G^*

buoyancy force between the two-phases causes small bubble rising velocity and slip ratio of the bubble relative to the liquid. The bubble was less deformed and the liquid film on the tube wall is thin. Because the capillary force near the mesh pores is large enough to balance the gravity force between the two-phases, the bubble interface is not sharp and the flow field near the bubble interface is gentle (see Fig. 5a).

As G^* is increased to 87.06, the buoyancy force is increased to speed up the bubble. The bubble is deformed to be elongated, with the increased liquid film thickness on the tube wall. The dynamic change of the flow field near the bubble interface is obvious. After some time evolution, the gravity force due to the two-phase density difference began to be larger than the capillary force created by the mesh pores, the gas-liquid interface will be protruded within the mesh pores (see Fig. 5b).

When G^* was further increased to 119.43, the bubble was accelerating significantly. The shear force between the two-phases thickens the liquid film on the tube wall and elongated the bubble length. The change of the flow fields at the bubble top and tail is more obvious. After a short time evolution, the bubble leakage happens (see Fig. 5c). Figure 5 identified the increased bubble rising velocities

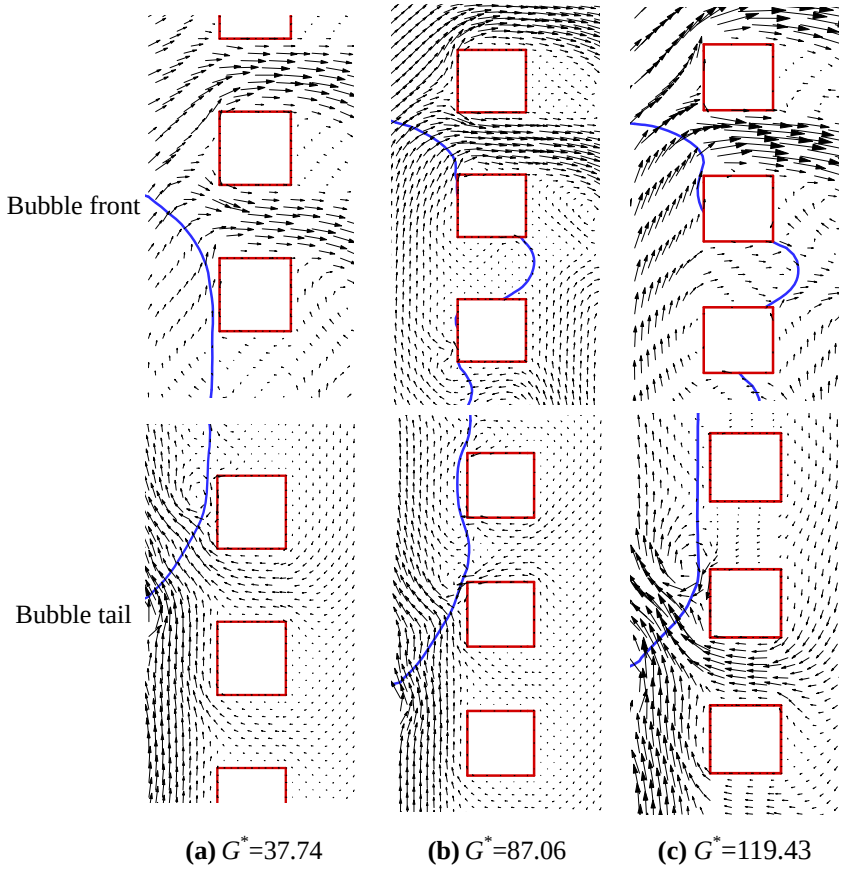

Fig. 6 The gas-liquid interface shape and flow field

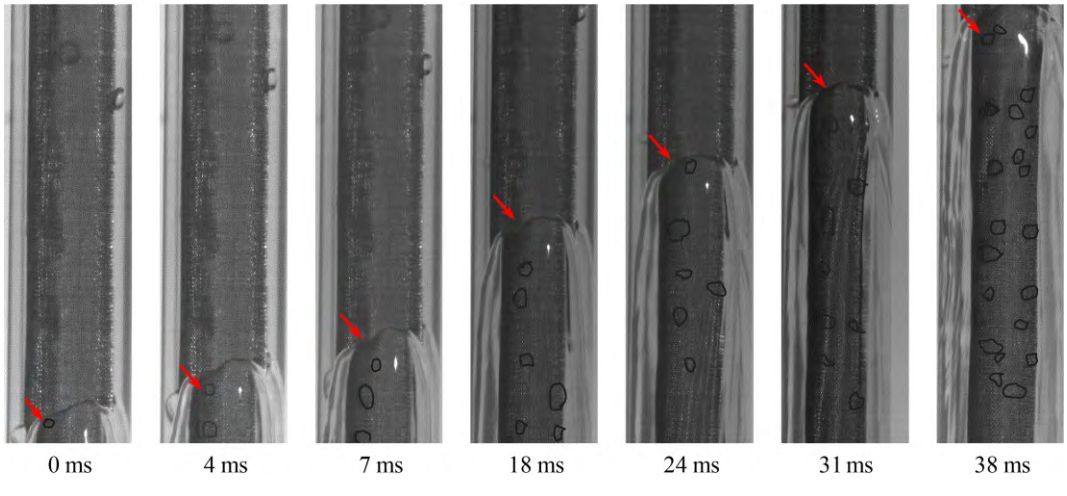

Fig. 7 Location of the bubble leakage [14]

and liquid film thicknesses on the tube wall with increases in G^* at the fixed *We* number. The bubble leakage happens more easily at larger G^*. This is because the gravity force due to the buoyancy force strongly depends on G^*.

Figure 6 shows the shape of the gas-liquid interface and the near-pore-flow-field at the bubble top and tail region at different G^*, in which the gas-liquid interface is represented by the blue color. The liquid velocities are increased and the gas-liquid interface is obviously deformed with increases in G^*. When the gravity force induced by the buoyancy effect is larger than the capillary force, the bubble interface breaks through the mesh pore. The

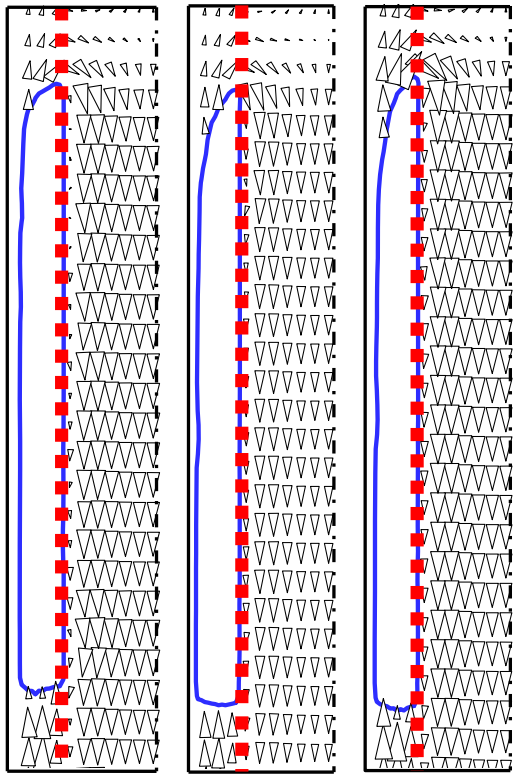

(a) *We*=1.0 **(b)** *We*=2.29 **(c)** *We*=3.0

Fig. 8 Bubble shape and velocity profile at different dimensionless *We* number

location of the bubble leakage takes place at the bubble top area that is close to the micromembrane surface, which is consistent with the experimental observations (see Fig. 7). This further proved the accuracy of the present numerical simulation.

Figure 8 explores the *We* number effect on the bubble shape and flow field at different G^*, in which Fig. 8a–c refer to the cases 1, 2 and 5, respectively. The *We* number definition tells us that *We* is inverse to σ. At *We*=1.0, even though the flow is violent near the bubble front and bubble tail, the gas-liquid interface is less deformed because the capillary force is large enough to balance the buoyancy effect induced gravity force (see Fig. 8a). As *We* is increased to 2.29, the gas-liquid interface is deformed with apparent interface curvature, under which the bubble leakage takes place (see Fig. 8b). The case of $We = 3.0$ enhances the bubble leakage phenomenon (see Fig. 8c). It is noted that the *We* number mainly influences the surface tension force. When *We* is increased to a specific value, the force balance on the gas-liquid interface is broken to emit miniature bubbles.

Figure 9 shows the gas-liquid interface and flow field near the bubble front and tail. The change of *We* number changes the surface tension force. The increase of *We* number decreases the surface tension force and deform the gas-liquid interface. The bubble leakage happens easily at large *We* number at the same G^*.

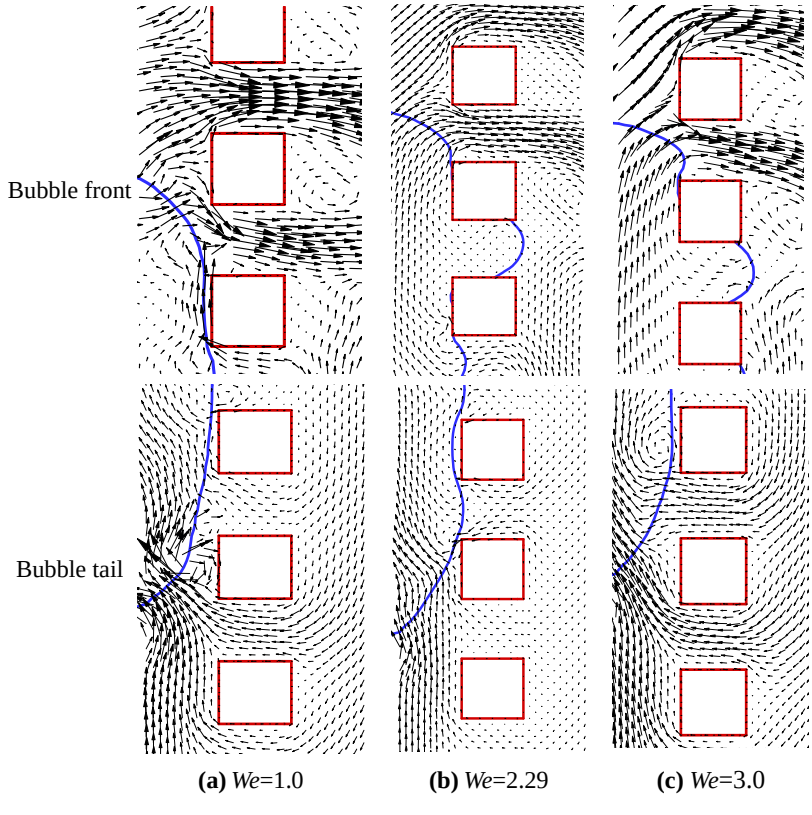

(a) *We*=1.0 **(b)** *We*=2.29 **(c)** *We*=3.0

Fig. 9 The gas-liquid interface and flow field near the bubble front and tail

4 Conclusion

The following conclusions can be drawn:

(1) The bubble dynamics were successfully modeled by applying the VOF method. The computation time is significantly shortened by the 3D to 2D conversion, the multiscale grid system and the frame of reference coordinate. These techniques overcome the difficulty of multiscale computations.

(2) The theoretical analysis found that the non-dimensional parameters G^*, We number and the coefficient C are the key parameters to determine if the bubble leakage occurs, in which C represents the influence of the inertia force, the viscous force and the pulsating flow. The numerical simulations identified the specific curve to distinguish the non-bubble-breaking cases and bubble-breaking cases, inferring the specific relationship between G^* and We number. The critical criterion for the bubble leakage is written as $G^* \times We = (0.22We^{0.99349} - \frac{G^*}{4.7\times10^3\times We^{0.00651}} + \frac{196.39}{We^{0.00651}}) \times \frac{4\cos\alpha}{\Delta\Theta W}$.

(3) The G^* value influences the buoyancy effect induced gravity force. The increase of G^* raises the gravity force to deform the gas-liquid interface and thicken the liquid film on the tube wall. The bubble leakage takes place when the gravity force is so large that it cannot be balanced by the capillary force. The We number affects the surface tension force. The increase of We number decreases the surface tension force. When We is increased to a specific value, the capillary force cannot balance the gravity force to break up the bubble front interface.

Acknowledgment This work was supported by the National Natural Science Foundation of China of International Cooperation Project (51210011), the National Basic Research Program of China (2011CB710703), the Young Scientists Fund of the National Natural Science Foundation of China (51106049) and the Fundamental Research Funds for the Central Universities (JB2013144).

References

1. Ma XH, Xu DQ, Lin JF (1999) Condensation heat transfer enhancement with dropwise and film coexisting condensation surface. CIESC J 50:535–540
2. Zhao Q, Lin JF (1991) Industrial application research progress of dropwise condensation. Chem Ind Eng Progr 42:17–20
3. Lang XQ, Ma HQ, Tan X (2004) Progress on dropwise condensation mechanismand heat transfer surface modification. J Petrochem Univ 17:32–38
4. Yang SM, Tao WQ (2006) Heat transfer, 4th edn. Higher education press, Beijing
5. Nusselt W (1916) Die Oberflachencondensation Der Wasserdampfes. VDI 60:541–569
6. Miyara A, Nonaka K, Taniguchi M (2000) Condensation heat transfer and flow pattern inside a herringbone-type micro-fin tube. Int J Refr 23:141–152
7. Sapali SN, Patil PA (2010) Heat transfer during condensation of HFC-134a and R-404A inside of a horizontal smooth and micro-fin tube. Exp Thermal Fluid Sci 34:1133–1141
8. Goto M, Inoue N, Yonemoto R (2003) Condensation heat transfer of R410A inside internally grooved horizontal tubes. Int J Refr 26:410–416
9. Olivier JA, Liebenberg L, Thome JR et al (2007) Heat transfer, pressure drop, and flow pattern recognition during condensation inside smooth, helical micro-fin, and herringbone tubes. Int J Refr 30:609–623
10. Uchida M, Itoh M, Shikazono N et al (1996) Experimental study on the heat transfer performance of a zeotropic refrigerant mixture in horizontal tubes. International Refrigeration and Air Conditioning Conference, Paper 313
11. Cavallini A, Del Col D, Doretti L et al (2000) Heat transfer and pressure drop during condensation of refrigerants inside horizontal enhanced tubes. Int J Refr 23:4–25
12. Muzzio A, Niro A, Arosio S (1998) Heat transfer and pressure drop during evaporation and condensation of R22 inside 9.52 mm O.D. micro-fin tubes of different geometries. Enhanced Heat Transfer 5:39–52
13. Chen HX, Xu JL, Wang W. An internal condenser tubes dispensing hood. Chinese Patent, 2011, CN102278904A
14. Chen HX, Xu JL, Wang W. An enhancement condensation pipe with inserted mesh cylinder. USA Patent, 2012, PCT/CN2012/000274
15. Chen HX, Xu JL, Li ZJ et al (2012) Stratified two-phase flow pattern modulation in a horizontal tube by the mesh pore cylinder surface. Appl Energy 112:1283–1290
16. Chen HX, Xu JL, Li ZJ et al (2012) Flow pattern modulation in a horizontal tube by the passive phase separation concept. Int J Multiph Flow 45:12–23
17. Chen HX , Xu JL, Xie J et al (2014) Modulated flow patterns for vertical upflow by the phase separation concept. Exper Thermal Fluid Sci 52:297–307
18. Taha T, Cui ZF (2002) CFD modelling of gas-sparged ultrafiltration in tubular membranes. J Membr Sci 210:13–27
19. Taha T, Cui ZF (2006) CFD modelling of slug flowin vertical tubes. Chem Eng Sci 61:676–687
20. Hung T, Lin LW (2002) Active microfluidic mixer and gas bubble filter driven by thermal bubble micropump. Sensor Actuat A 97-98:665–671
21. Lemenand T, Dupont P, Valle DD et al (2013) Comparative efficiency of shear, elongation and turbulentdroplet breakup mechanisms: Review and application. Chem Eng Res Design 91:2587–2600
22. Conrath M, Smiyukha YL, Fuhrmann E et al (2003) Double porous screen element for gas–liquid phase separation. Int J Multiph Flow 50:1–15
23. Federico M, Fernando AM (2012) Multiphase capillary flows. Int J Multiph Flow 42:62–73
24. Chen QC, Xu JL, Sun DL et al (2013) Numerical simulation of the modulated flow pattern for vertical upflows by the phase separation concept. Int J Multiph Flow 56:105–118